ARTICLE

Check for updates

Widely-tunable, multi-band Raman laser based on dispersion-managed thin-film lithium niobate microring resonators

Yanjing Zhao[1,3], Xiaoyue Liu [2,3], Kresten Yvind [1], Xinlun Cai [2✉] & Minhao Pu [1✉]

Stimulated Raman scattering is an attractive way to extend the operation spectral range of optical sources. However, the spectral extension range of a tunable Raman laser is limited by the Raman frequency shift and pump tuning bandwidth. This makes it challenging to realize chip-scale, widely tunable Raman lasers, as on-chip lasers only provide limited pump power and tuning bandwidth. Here, we tackle this by dispersion engineering of a thin-film lithium niobate microring resonator, where its high-quality factor (~ 2.5 million) ensures a sub-milli-watt (0.8 mW) threshold for Raman lasing while its strong normal dispersion with sup-pressed avoided mode crossing restrains the competing Kerr comb generation process. Combining the multi-wavelength Raman gain response of lithium niobate and cascaded Raman lasing, we demonstrate a widely tunable Raman laser covering 1592–1955 nm, showing a 335-nm spectral extension range from a 94-nm-tuning-bandwidth pump laser. Our demonstration paves the way to realize chip-scale, widely-tunable Raman lasers.

[1] DTU Electro, Department of Electrical and Photonics Engineering, Technical University of Denmark, Lyngby, Denmark. [2] Key Laboratory of Optoelectronic Materials and Technologies and School of Electronics and Information Technology, Sun Yat-sen University, Guangzhou, China. [3] These authors contributed equally: Yanjing Zhao, Xiaoyue Liu. ✉email: caixlun5@mail.sysu.edu.cn; mipu@dtu.dk

Stimulated Raman scattering (SRS) is an attractive nonlinear process to extend the available spectral range of conventional lasers[1,2]. The Stokes radiation can be generated at the Raman frequency shift related to the phonon vibration of the material by high-power pumping nonlinear Raman medium[3]. Developing integrated high quality-factor (Q) microresonators relaxes the required pump level for Raman lasing, enabling continuous-wave (CW) pumping operation[4]. Integrated Raman lasers have been demonstrated using various materials such as silicon[5,6], chalcogenide[7], aluminum nitride[8], diamond[9,10], and silicon carbide[11]. They exhibit compactness, low pump threshold, and large design freedom, allowing for applications in spectroscopy, sensing, and medical diagnosis[12–14].

The wavelength tuning of the Raman lasers is desired in those applications and can be realized by changing the pumping wavelength[7,8,10,15,16]. The spectral extension range from the pump laser determines the effective tuning range of a Raman laser, and it is usually limited by either the Raman frequency shift or the pump tuning bandwidth (see Supplementary Note 1). For most integrated Raman lasing demonstrations, the material platforms only possess one strong Raman vibration phonon branch, and the achieved effective tuning ranges of the Raman lasers are limited to less than 100 nm. To realize an effective tuning range beyond 100 nm, three different pump lasers were required for a widely-tunable Raman lasing in a silicon multimode concentric racetrack resonator[15]. However, achieving such a wide tuning range for chip-scale Raman lasers is not trivial because multiple on-chip tunable pump laser sources are required to integrate and cooperate with a single microring resonator. Besides, a sophisticated device design concerning pump-to-resonator coupling is also needed for broadband high-Q operation[15]. Cascaded Raman scattering can also be employed to extend the Raman tuning ranges[7,8,17] but with a compromised conversion efficiency of the high-order Raman scattering. Alternatively, one can use multi-Raman-response materials[18–22] such as lithium niobate (LN)[23–27]. However, as LN also exhibits a strong Kerr effect, the previously demonstrated Raman lasing in LN microresonators competes with Kerr comb generation (KCG) and four-wave mixing (FWM) processes, and no tunable Raman lasing has been demonstrated[28]. In addition, they observed a high threshold up to 20 mW, making it challenging to drive the Raman laser using on-chip lasers. To suppress the FWM-related parametric amplification triggered by the pump and the Raman response[29], the microresonators must be designed in the normal dispersion region at the pump and its corresponding Raman frequencies. For normal-dispersion microresonators, any mode hybridization induced by inter-mode coupling will result in the avoided mode crossing (AMX)[30]. Such AMX not only alters the local dispersion to enable the parametric amplification for KCG[30–34] but also leads to Q degradation[35–37], thus increasing the Raman lasing threshold. Since the multi-mode waveguide dimensions are usually used for suppressing scattering loss for fundamental modes, it is critical to suppress AMX in multi-mode micro-resonators to ensure low threshold and KCG-free operation for tunable Raman lasing.

In this work, we demonstrate a thin-film LN (TFLN) microring resonator, where a multi-mode waveguide dimension ensures high Q (around 2.5 million) while the dispersion management ensures a strong normal dispersion operation with suppressed AMX. Thanks to the suppression of KCG, we take advantage of LN's multi-wavelength Raman gain response and demonstrate Raman lasing with an effective tuning range of 335 nm by sweeping the pump wavelength within less than 100 nm. Moreover, we also achieve a sub-milli-watt threshold for the Raman lasing.

Results

Design for KCG-suppressed TFLN microresonators. LN has attracted significant interest for its large nonlinear-optic, electro-optic, and piezoelectric coefficient[38–40]. Bulk LN crystal[41–44] and weakly confined waveguides[45–49] have been widely used for decades, while the emergence of thin-film LN (TFLN)[50–54] enables strong light confinement and provides a new opportunity for wafer-scale integrated photonic devices with high nonlinearities[55]. Benefited from recent fabrication advances in low-loss TFLN waveguides and microresonators, a large land-scape of nonlinear phenomena have been explored in this plat-form, including optical frequency comb generations[56–59], electro-optic modulators[60–62], optical parametric amplification[63,64], frequency doublers[53,65–69], optical switch[70] and erbium-doped lasers or amplifiers[71]. Raman lasing has been demonstrated in LN whispering-gallery-mode resonators[72–76] and TFLN microring resonators[28]. However, the tunable property of Raman lasing has not been demonstrated because of the competing nonlinear FWM processes (or KCG)[77,78] due to its high Kerr nonlinearity. Here, we design a KCG-suppressed TFLN microring resonator for tunability.

A schematic of the TFLN microring resonator-based Raman laser is shown in Fig. 1a. A high-Q TFLN microring resonator enhances the intracavity pump power and thus reduces the Raman threshold. Benefiting from the multiple Raman-active phonon branches of the LN material, multi-wavelength Raman lasing can be generated when both the pump and its Stokes frequencies are aligned to the resonances of the microring resonator. Meanwhile, the generated Stokes lines can also act as new pumps to induce cascaded Raman lasing, further extending the wavelength range of Raman lasing. Besides the Raman response, there is also the Kerr effect in high-Q microresonators, which would compete with Raman lasing and degrade the Raman efficiency. Kerr frequency combs can be generated via modulational instability-induced nonlinear optical parametric oscillations in microresonators with global anomalous dispersion (green dots in Fig. 1b) or local anomalous dispersion (blue dots in Fig. 1b). In the latter case, the local anomalous dispersion can result from the AMX, which may periodically induce a resonance shift and cause local dispersion deviation. Once the dispersion deviation is sufficient to compensate for the original normal dispersion and cause a local anomalous dispersion, KCG is triggered[30,32,34,37]. As the tuning of a resonator-based Raman laser is realized by pumping different resonances, the periodical AMX-induced KCG will prohibit the Raman tuning operation. The AMX period is determined by the group index difference of the coupled modes, shown in Fig. 1c, where the blue curves represent the resonances of the fundamental mode in the microresonators. Such AMX would also reduce the Q of microring resonators and increase the threshold for Raman lasing[15]. Therefore, the normal dispersion without AMX (red in Fig. 1b) is desired for tunable Raman lasers.

Single-mode waveguide design can be used to avoid intermodal coupling and thus the associated AMX. However, multi-mode waveguide designs are preferable to achieve a high Q for strong nonlinear enhancement as the fundamental mode can be isolated better from the sidewall roughness[50]. In this case, the AMX induced by intermodal coupling becomes inevitable, especially over a large frequency range. Nevertheless, the KCG can still be suppressed if the AMX-induced dispersion deviation is not large enough to compensate for the original normal dispersion[32,34,37]. Therefore, to suppress the competition between KCG and Raman lasing, the occurrence number of AMX and the intermodal coupling strength should be limited while the overall dispersion should be relatively strong. Suppressing intermodal coupling strength also helps avoid Q degradation of the fundamental
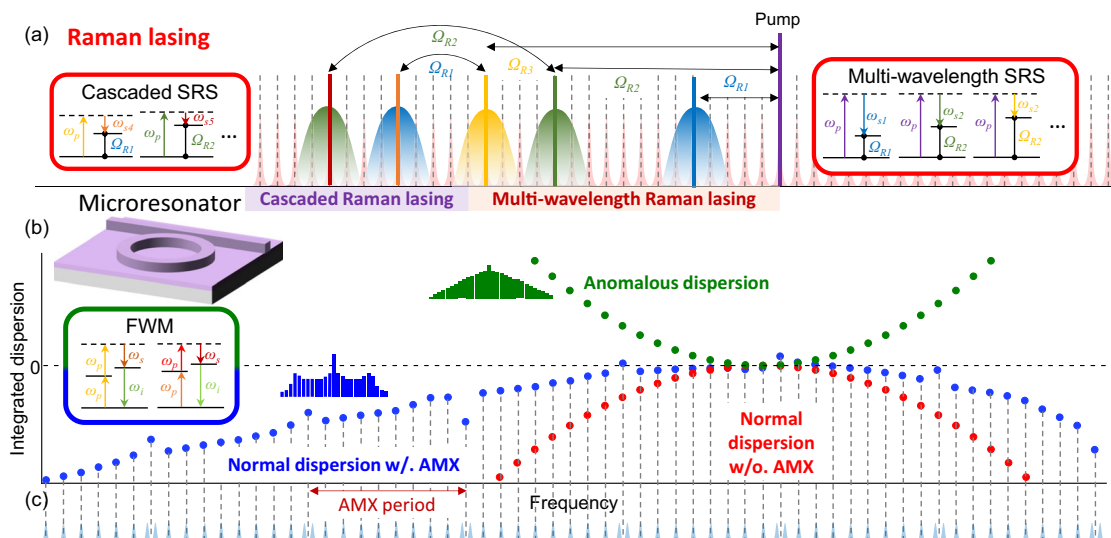
Fig. 1 Operation principle of the tunable multi-band Raman laser. Suppression of the competing nonlinear FWM in thin-film lithium niobate (TFLN) microring resonators for Raman lasing. **a** A schematic example of the multi-band Raman lasing where the multiple Raman-active phonon branches of lithium niobate (LN) lead to multi-wavelength Raman lasing while the generated Stokes lines can also act as new pumps to induce cascaded Raman lasing, further extending the Raman lasing range. The gradient lobes represent the Raman gain envelope with the Raman frequency shifts Ω_{Ri} (i = 1, 2, 3...). **b** The integrated dispersion profile in three different dispersion regions. The competing nonlinear FWM process may lead to Kerr comb generation in a TFLN microring resonator (inset) for both anomalous dispersion (green) and normal dispersion with avoided-mode crossing (AMX) (blue). In contrast, the device with normal dispersion without AMX (red) can suppress the nonlinear FWM and thus favor its counterpart process: Raman lasing. **c** Schematic resonances of the fundamental mode of a multi-mode microresonator (corresponding to the blue dispersion in **b**) influenced by the AMX. The inter-mode coupling would induce resonance shift and cause a periodic dispersion deviation around AMX points, where the group index of the coupled modes determines the AMX period.

mode, thus ensuring a low threshold for Raman lasing. Finally, one also needs to consider the effective mode area, as the mode confinement also affects the nonlinear efficiency[79]. Therefore, to achieve a low-threshold, widely tunable Raman laser, a resonator waveguide design featuring (1) a small effective mode area, (2) a strong normal dispersion, and (3) suppressed AMX is highly desirable.

The schematic cross-section of a TFLN waveguide is depicted in Fig. 2a, which is defined by waveguide height (H), waveguide width (W), sidewall angle (θ), and etch-depth (h). Figure 2b shows an example where both TE_{00} and TE_{10} modes exist in a TFLN waveguide ($W = 2.2\,\mu m$, $H = 360\,nm$, $h = 180\,nm$, and $\theta = 60°$). Figure 2c shows the calculated effective mode area (color-shaded contour) and group velocity dispersion (GVD) (black contour lines) of the TE_{00} mode for different waveguide heights (H) and widths (W), with $h = H/2$, and $\theta = 60°$. It is seen that the effective mode area reaches a minimum when the waveguide height is reduced to 360 nm, and the waveguide dispersion moves to strong normal dispersion as the waveguide height is reduced. The 360-nm thick waveguides exhibit a strong normal dispersion (about $-500\,ps\,nm^{-1}\,km^{-1}$), much stronger than those waveguides used for KCG in[30–33,80,81].

Fixing the waveguide height to 360 nm, we also investigate how the AMX can be suppressed concerning its intermodal coupling strength and occurrence within the wavelength range of 1500–2000 nm (covering both the pump and Raman laser wavelength tuning ranges). The occurrence number of AMX depends on its period, which is related to the group index of both modes[82] (detailed in Supplementary Note 2). Depicted as the red-line contour in Fig. 2d, the occurrence number of AMX increases significantly with the etching depth. The intermodal coupling strength depends on the phase matching condition or the effective refractive index difference, indicated by the blue-line contours in Fig. 2d[83,84]. With the refractive index difference between TE_{00} and TE_{10} modes increasing, the intermodal

coupling can be better suppressed. Figure 2d also shows the effective mode area as a color-shaded contour. Unfortunately, no single operation region fulfills all the requirements mentioned above. In that, operating a waveguide in the upper left part of Fig. 2d is ideal concerning the effective mode area and the index difference, while working in the bottom left region is favored for limiting the occurrence of AMX. Besides, a relatively large width is needed for the multimode waveguide to ensure a high-Q operation (see Supplementary Note 3). Here, we use a waveguide design ($W = 2.2\,\mu m$, $H = 360\,nm$, $h = 180\,nm$, and $\theta = 60°$) labeled as the red star in Fig. 2d to balance those parameters for tunable Raman lasers. The tunability of the Raman laser will be affected by the occurrence number and the intensity of AMX, which are determined by the etching depth and waveguide width, respectively (see Supplementary Note 4). Therefore, over-etching and oversized waveguide patterning should be avoided to prevent decreased tunability.

Linear characterization of microresonators. A scanning electron microscopy (SEM) picture of a fabricated 100-μm-radius TFLN microring resonator is presented in Fig. 3a. Figure 3b, c shows SEM pictures of the coupling region of a microring resonator with a 1-μm-wide coupling gap, and the cross-section of a TFLN waveguide (W = 2.2 nm, H = 360 nm, h = 180 nm, and θ = 60°), respectively. We characterized 31 TFLN microresonators with the same waveguide design. A typical transmission spectrum of the microresonators is shown in Fig. 3d, where the red (blue) resonances represent the TE_{00} (TE_{10}) mode. The insertion loss of TE_{00} mode is 4.3 dB.

As the waveguide dispersion is engineered so that the occurrence of AMX is limited to three within the wavelength range of 1500–2000 nm, we only observed one AMX within our transmission measurement range (1500-1630 nm) for all the devices. The resonance responses around the AMX are shown in
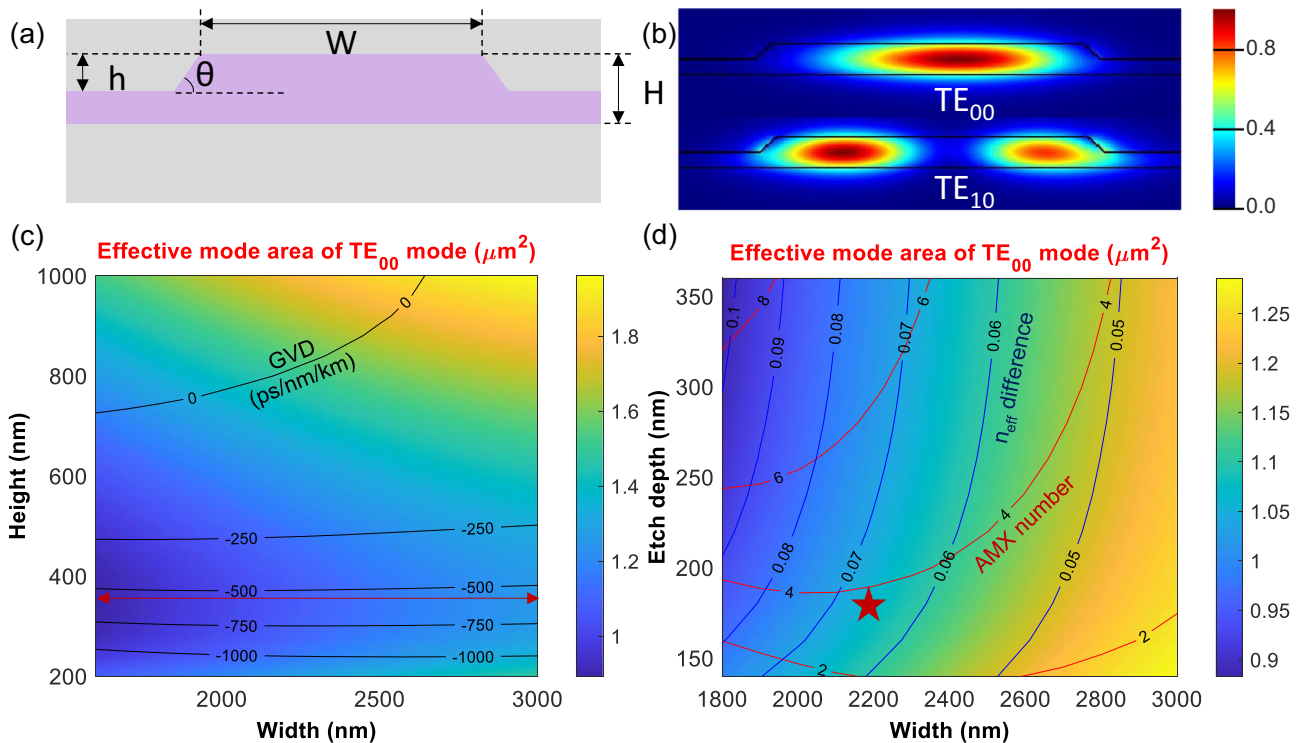
Fig. 2 Dispersion management of the TFLN waveguide for AMX-suppressed microresonators. a The schematic cross-section of the TFLN waveguide which is defined by a waveguide height (H), a waveguide width (W), a sidewall angle (θ), and an etch depth (h). **b** The TE_{00} and TE_{10} mode profiles in a 2.2-μm-wide LFTN waveguide ($H = 360$ nm and $h = 180$ nm). **c** Color: The effective area of TE_{00} mode versus the waveguide height (H) and waveguide width (W) ($h = H/2$). The black contours indicate the group velocity dispersion (GVD) of TE_{00} mode. **d** Color: The effective area of the TE_{00} mode versus the etching depth (h) and waveguide width ($H = 360$ nm). The blue contours represent the effective refractive index difference of TE_{00} and TE_{10} modes, and the red contours are the occurrences of AMX within the pump and Raman lasing tuning range (1500–2000 nm).

Fig. 3e, where one can find that the Qs are maintained around 2 million for the TE_{00} mode. The histogram of measured Q for TE_{00} mode is presented in Fig. 3f, showing an average intrinsic Q of around 2.5 million. The integrated dispersion can be extracted from the transmission[85] as depicted in Fig. 3g. Here the dots indicate the measured results, while the curve represents the fitted dispersion profile. The derived GVD is -526 ps nm^{-1} km^{-1} at 1550 nm, inferring a strong normal dispersion, which agrees well with the calculated GVD profile shown in Fig. 3h. All normal dispersion is maintained within the 800–2000 nm wavelength range. The arrows in Fig. 3h indicate the AMX wavelength calculated based on the measured point in Fig. 3d and the AMX period, showing that those AMX wavelengths are in a deeper normal dispersion region than the pump wavelength.

Blue dots in Fig. 3g show the integrated dispersion of TE_{10} mode with respect to the FSR of TE_{00} mode at 1550 nm. As the wavelength increases from 1584 nm to 1594 nm, the two modes gradually approach and cross each other, thus introducing an AMX around 1588 nm. We extract the resonance frequency deviation by comparing the measured data and the fitted curve at the AMX resonance wavelength. As the waveguide exhibits a modest effective index difference between TE_{00} and TE_{10} modes, the intermodal coupling is suppressed[84]. The average frequency deviation at the AMX resonance for all 31 devices is about 200 MHz, with several devices showing few-MHz frequency deviations. Figure 3g presents an example showing almost negligible frequency deviation (8 MHz) at the AMX resonance. Such AMX-induced frequency deviation cannot compensate for the strong normal dispersion to get local anomalous dispersion. The influence of AMX is detailed in the Supplementary Note 4. Therefore, KCG can be suppressed during the tuning operation of the Raman laser.

Low Raman lasing threshold. Subsequently, the Raman characterization was conducted for the TFLN microring resonators. Figure 4a shows the Raman emission spectrum when the resonator is pumped with 32-mW on-chip power around 1546 nm. Unlike other traditional Raman lasing materials, LN has several strong vibrations phonon branches[11,28]. For the TE polarization, we can observe three Raman oscillations with frequency shifts of 253 cm^{-1}, 631 cm^{-1}, and 875 cm^{-1}, which correspond to the optical phonon branches of $A(TO_1)$, $A(TO_4)$ and $A(LO_4)$, respectively. The measured Raman lasing thresholds of the three Stokes lines are presented in Fig. 4b–d, where the pump detuning is optimized to maximize each Stokes line power for each data point. Benefiting from the high-Q microresonators, we achieved a sub-milli-watt-level threshold (0.8 mW) for the 1st Stokes line. As far as we know, this is the lowest Raman lasing threshold reported in the TFLN platform. Above the threshold, the Stokes light is enhanced with pump power increasing. The slope efficiency is estimated to be about 8.65% by linearly fitting the measured data points above and close to the threshold. Extracted similarly, the thresholds for the second and third Stokes lines are 2.7 mW and 24 mW, with slope efficiency of 8.51% and 5.30%, respectively. Among the three Stokes frequencies, the 1st Stokes line ($A(TO_1)$) has the largest Raman gain coefficient while the 3rd Stokes line ($A(LO_4)$) has the lowest Raman gain coefficient[24]. Besides, a smaller mode overlap and a decreased intrinsic Q are expected at a longer wavelength range. Therefore, the Raman lasing threshold increases from the 1st Stokes line to the 3rd Stokes line. The conversion efficiency difference is attributed to the wavelength dependence of the mode overlap and the resonator coupling condition. Operating the resonator at the over-coupling condition can lead to a higher slope efficiency but with an increased Raman
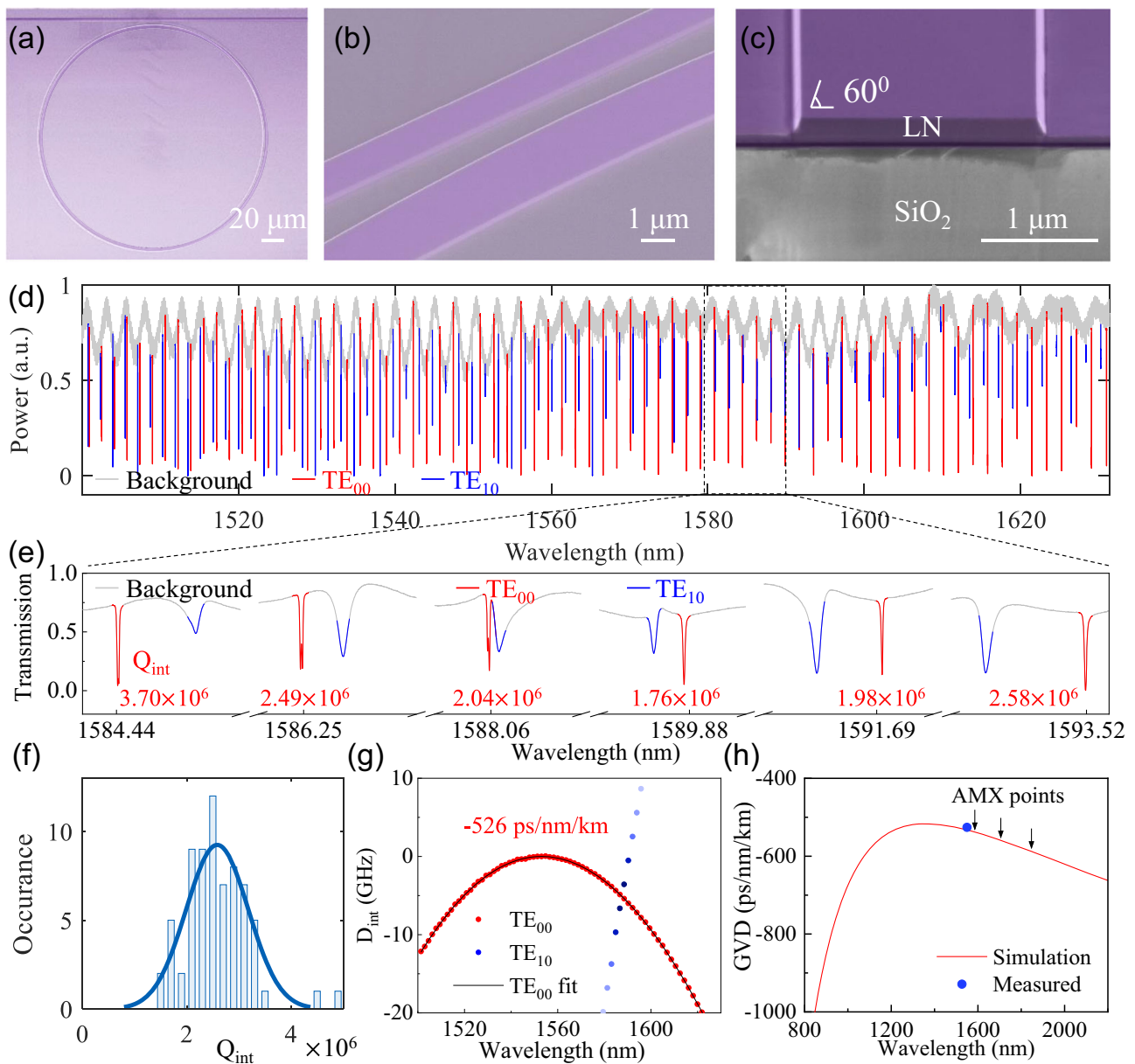
Fig. 3 Characterization of the Q and dispersion of TFLN microresonators. Scanning electron microscopy (SEM) images of **a** a 100-μm-radius TFLN microring resonator, **b** the coupling region with a 1-μm-wide coupling gap and 1.2-μm-wide bus waveguide, and **c** the cross-sectional view of the TFLN waveguide (*W*: 2200 nm, *H*: 360 nm, *h*: 180 nm, *θ*: 60°). **d** Transmission spectrum of the microring resonator. **e** Enlarged view of **d** around the AMX wavelength. **f** Histogram of measured intrinsic Qs for the TE_{00} mode. **g** Measured integrated dispersion of the TE_{00} and TE_{10} modes with respect to the FSR of TE_{00} mode at 1550 nm. The TE_{00} mode only has an 8-MHz frequency deviation from the fitted curve. **h** Simulated GVD profile of the TFLN waveguide, the blue point is the derived GVD from **g**, and the arrows are the estimated AMX wavelengths.

lasing threshold. There is a trade-off between the slope efficiency and the threshold. It's worth mentioning that the 1st Stokes line exhibits a relatively low saturation power, primarily attributed to the presence of competing Stokes lines or Raman oscillations[4] occurring within the broad gain bandwidth of the phonon branch (A(TO1)) associated with the 1st Stokes line. Compared to the previously reported LN Raman laser[28], our work demonstrated a much lower threshold.

Broadband tunability of the Raman laser. To investigate the tunability of the Raman laser, we further increased the pump power to around 52 mW, where we can get two extra cascaded Stokes lines, as shown in purple and orange spectra in Fig. 5a. The

observed fourth (fifth) Stokes line highlighted by the bold purple (orange) is a result of a cascaded process with a Stokes frequency shift of 254 cm^{-1} (624 cm^{-1}) from the third (second) Stokes line highlighted by the bold green (blue) line, which corresponds to the optical phonon branches of A(TO$_1$) (A(TO$_4$)). The threshold and slope efficiency of the cascaded Stokes lines are detailed in Supplementary Note 5. All these five Stokes lines can be shifted accordingly by consecutively tuning the pump light into different resonances. We tune the pump wavelength within the telecom C-and L-bands (1526-1620 nm). The wavelength tuning step equals the FSR of the microring resonator, namely around 1.68 nm.

All the Raman spectra are recorded in Fig. 5a, demonstrating the tuning range for all five Stokes groups as 1592–1685 nm,
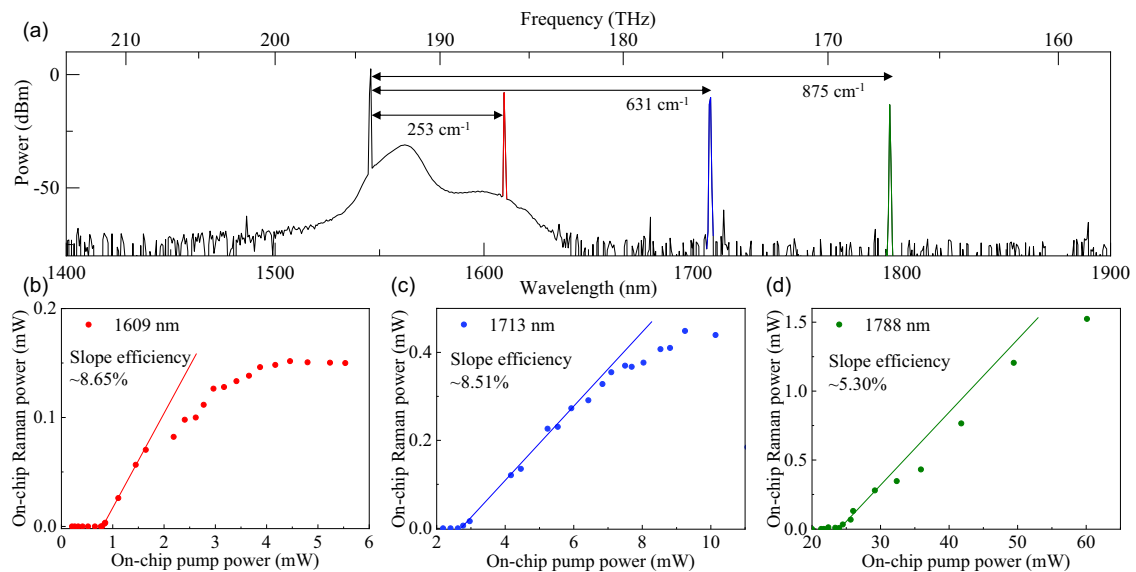
Fig. 4 Multi-wavelength Raman lasing characterization. a Multi-wavelength Raman lasing spectrum around 1609 nm, 1713 nm, and 1788 nm with a 253 cm^{-1}, 631 cm^{-1}, and 875 cm^{-1} Raman shift, respectively, from the pump 1546 nm (on-chip pump power ~32 mW). **b–d** Measured on-chip Raman power at the first **b**, the second **c**, and third **d** Stokes frequency versus on-chip pump power. A sub-milliwatt-level threshold (0.8 mW) is observed for the Raman lasing at the first Stokes frequency.
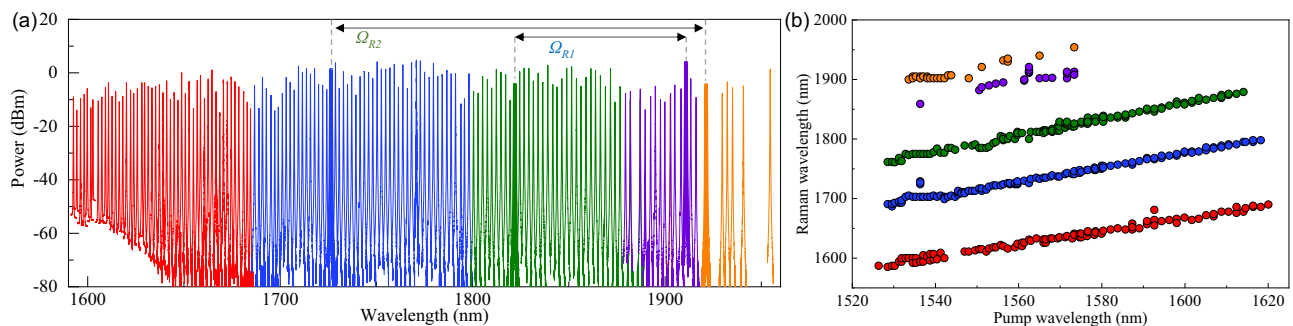

Fig. 5 Tunability of the multi-band Raman laser. a The measured spectra of the 1st (red), 2nd (blue), and 3rd (green) Stokes lines and the cascaded Raman branches (purple and orange) by discrete tuning the pump wavelength from 1526 nm to 1620 nm. The pump power is kept below 52 mW during the wavelength sweep. **b** The measured Raman lasing wavelength of the five groups versus the pump wavelength.

1687–1798 nm, 1800–1877 nm, 1879–1921 nm, and 1929–1955 nm. The five Stokes lines may require different pump-to-resonance detuning for pumping the same resonance to reach maximum intensity. Thus, the pump detuning is optimized separately to guarantee the maximum emission of each Stokes line. The signal-to-noise ratio (SNR) is around 80 dB for the multiband Raman response (see Supplementary Note 6). The relationship between the Raman lasing wavelength and pump wavelength is illustrated in Fig. 5b. Generally, the Raman wavelength increases with the pump within each group. For the first three Stokes groups, which are directly generated by the pump, the Raman lasing is absent for a few pump resonances (for example, the first Stokes peak is missing for the pump wavelength around 1545 nm) while the corresponding missing Raman lasing wavelength can be still covered by careful control the pump-to-resonance detuning at other nearby resonances (for example, those resonances around 1540 nm). For the fourth and the fifth Stokes groups, there are indeed several gaps between the Stokes lines since the cascaded Raman process requires a higher threshold, which can be larger than the pump power used in the experiment. Therefore, the Raman lasing wavelength can be consecutively tuned from 1592 to 1921 nm and extended to 1955 nm. Here, we observed the output power fluctuates within each of the Stokes groups since (1) the actual pump power is not constant, which is induced by the amplification envelope of the erbium-doped fiber amplifier; (2) the fiber-to-chip coupling loss varies with the wavelength; (3) local fabrication defects may also degrade the Q for specific resonances. Further improvement can be expected by optimizing the fabrication process and special design for broadband flat coupling.

Large Raman output power. The highest Raman power in Fig. 5a is achieved in the 2nd Stokes group with pump wavelength ~1594 nm and on-chip pump power 41 mW. By pumping the resonance around 1594 nm, we then measured on-chip Raman power of the 2nd Stokes line vs pump power, as depicted in Fig. 6a. With 58-mW pump power, we achieved the largest Raman output power of 12.3 mW around 1773 nm. The corresponding spectrum is shown in Fig. 6b, showing good suppression of comb generation even at the highest Raman power. The output spectra at different pump power and detuning are detailed in Fig. S6 in Supplementary Note 7. Besides, Fig. 6a shows a large slope efficiency of 36.23% but a high threshold of 13.7 mW. The large slope efficiency requires the over-coupled condition while
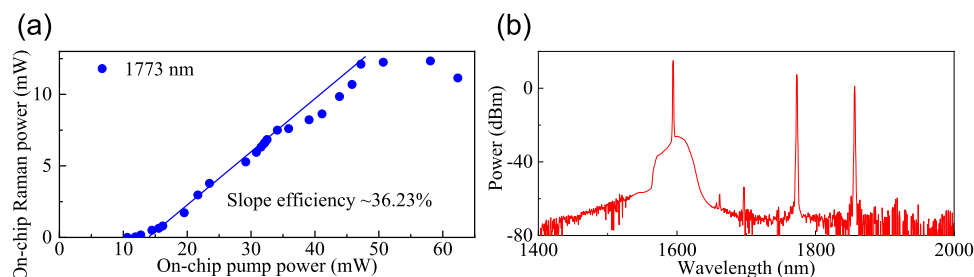
Fig. 6 Large Raman output power. a On-chip Raman power of the 2nd Stokes line versus pump power when pumping around 1594 nm, the blue dots represent the experimental results and the blue line represents the linear fitting to extract the slope efficiency; **b** the spectrum of the maximum Raman output power, showing 12.3-mW output power of the 2nd Stokes line.

Table 1 Comparison of widely tunable Raman laser based on microresonators.

Platform	f_{Raman} (THz)	On-chip threshold (mW)	Slope efficiency	Maximum Raman power (mW)	Pump tuning range (nm)	Raman tuning range (nm)	Spectral extension range (nm)	Ref.
As_2S_3	10.3	3[#]	—	—	1522–1574	1610–1663	53	2
GeSbS	10.2	3.25	13.86%	0.2	1535–1570	1615–1658	43	7
AlN	18.3	8	3.6%	4.35	1500–1630	1700–1790	90	8
Diamond	40	85	0.43%	0.25	—	1950–2050	100	10
Si	15.6	0.3	8.5%	0.02	1240–1680	1325–1841	161	15
LN	7.6[*]	0.77	36.23%	12.3	1526–1620	1592–1955	335	This work

[*]The first Raman frequency shift. The second and third Raman frequency shifts for lasing are 18.9 and 26.2 THz, respectively. The two cascaded Raman frequency shifts for lasing are 33.8 and 37.6 THz.
[#]The work is done in an As_2S_3 chalcogenide glass microsphere. The threshold is the pump power before the silica taper.

the low threshold requires the critical-coupled condition of the pump resonance, so there is a trade-off between the two parameters[79]. While the maximum Raman power is larger in the former LN demonstration, it is obtained by a much stronger pump (400 mW) with the co-existence of KCG[28]. In our work, the waveguide is tailored to guarantee low-loss and strong normal dispersion with suppressed AMX. Therefore, a KCG-free operation is obtained for Raman lasing with a 12.3-mW Raman output power.

Discussion

Table 1 highlights the performance of microresonator-based tunable Raman lasers from different integrated platforms, including As_2S_3[2], GeSbS[7], AlN[8], diamond[10], Si[15], and LN. Thanks to the nonlinear enhancement from high-Q resonators, Raman lasing can be achieved with sub-hundred milli-watt thresholds in those platforms. Sub-milli-watt level threshold has been achieved in the silicon platform. However, the TPA-induced free carrier absorption must be suppressed in silicon via carrier sweeping, which adds complexity to the fabrication process[15]. Since TFLN is TPA-free in the telecom wavelength, as long as the patterning processes ensure a high Q and the dispersion management prevents KCG, a low threshold Raman laser can be achieved, as we demonstrated in this work. The output power of those Raman lasers is typically limited to a sub-milli-watt level, while the milli-watt-level output power is reported in the AlN[8], Si[17] platform and this work.

The tuning range of Raman lasing depends on the pump tuning range. The tuning operation for most of the Raman lasers[2,7,8,10] listed in Table 1 relies on only one pump laser, which prevents the Raman tuning range beyond 100 nm. For these devices with only one strong Raman vibration phonon branch, although the tuning range can be further extended when one can sweep the pump over a larger spectral range by combining multiple tunable lasers, the maximal spectral extension range

from the pump source is determined by the Raman frequency shift. For instance, although the Raman wavelength can be tuned from 1325 nm to 1841 nm in a silicon Raman laser[15], about 70% of the demonstrated Raman tuning range overlaps with its pump tuning range. The achieved spectral extension range from its pump (or the effective tuning range) is limited to 161 nm, corresponding to silicon's Raman frequency shift (15.6 THz). Therefore, materials with larger Raman frequency shifts, such as diamond (with $f_{Raman} = 40$ THz), are favored for achieving a larger effective tuning range for Raman lasers if broadband pump sweeping is accessible by using, e.g., multiple tunable pump sources. However, realizing its fully integrated version is very challenging due to the difficulty of integrating and cooperating with multiple pump laser sources with a single microring resonator.

In contrast, utilizing the multi-wavelength Raman response of LN and cascaded Raman lasing, we relaxed the tuning bandwidth requirement on the pump laser and broke the spectral extension range constraint imposed by the Raman frequency shift in this work. We managed to achieve a substantial spectral extension range in Raman lasing, spanning 335 nm, despite having a relatively narrow tuning bandwidth (94 nm) of the pump laser. It makes TFLN a promising platform to realize fully-integrated, widely-tunable Raman lasers. Note that the tuning operation in these microresonator-based lasers is typically discrete, with a tuning step that equals one or several FSRs of the resonators. Thermal tuning can be applied to realize a continuous tuning operation[86,87].

Conclusions

In conclusion, we have presented a generic dispersion management scheme to design a high-Q, KCG-suppressed microresonator for Raman lasing and a simple way to significantly extend the tuning range of Raman laser beyond that of the pump laser for materials with multiple Raman responses. We have

demonstrated a widely tunable, multi-band TFLN Raman laser with its operation power within reach of on-chip lasers[88–91]. Our demonstration paves the way for the realization of fully integrated broadband Raman lasers, which will further promote the development of applications in spectroscopy and sensing.

Methods

Dispersion calculation. We use the commercial software Ansys Lumerical Mode Solutions to build the model of TFLN microring resonator for dispersion engineering. As LN is characterized as a negative uniaxial material with distinct ordinary and extraordinary refractive indices (n_o and n_e), we conduct separate simulations to determine the effective refractive index (n_{eff}) of the TE_{00} and TE_{10} modes for both n_o and n_e. The calculation of group velocity dispersion (GVD) is based on the equation $\beta_2 = \partial^2\beta/\partial\omega^2$, where β represents the propagation constant ($\beta = 2\pi n_{eff}\lambda$) and λ denotes the wavelength. Subsequently, the GVD parameter is determined using $GVD = 2\pi c\beta_2\lambda^2$, where c is the speed of light. The sample is based on an X-cut wafer, and for the TE polarization, we utilize both n_o and n_e since the TE light experiences varying refractive indices while circulating within the resonator. To account for the ring structure, the GVD for the TE polarized mode is further refined by incorporating 50% of the GVD of n_o and 50% of the GVD of n_e.

Device fabrication. The devices are fabricated on an X-cut lithium niobate-on-insulator (LNOI) wafer from NANOLN. The thicknesses of the LN and buried oxide layers are 360 nm and 4.7 μm, respectively. Electron beam lithography (EBL) is employed to define the waveguides on a hydrogen silsesquioxane (HSQ) resist. Subsequently, the defined patterns are transferred to the LN layer through inductively coupled plasma (ICP) dry etching, resulting in an etching depth of 180 nm. A second EBL step followed by ICP dry etching are utilized to form the strip waveguides for the edge coupler. Finally, a 2-μm-thick SiO_2 layer is deposited onto the wafer as the upper-cladding layer using plasma-enhanced chemical vapor deposition (PECVD).

Experiment setup. The driving laser used for Raman lasing is a commercially available C + L-band laser (Toptica CTL 1570). The laser is amplified by a C-band (or L-band, depending on the pump wavelength) EDFA, its polarization is aligned to the TE mode of the device using a polarization controller (PC), and the pump power can be controlled by an attenuator. Two 20-dB couplers are used before and after the device to monitor the input and output power. The output spectra are recorded by an optical spectrum analyzer (OSA, YOKOGAWA AQ6375). The experimental setup is depicted in the Supplementary Note 8.

Reporting summary. Further information on research design is available in the Nature Portfolio Reporting Summary linked to this article.

Data availability

References

1. Rong, H. et al. A continuous-wave Raman silicon laser. *Nature* **433**, 725–728 (2005).
2. Andrianov, A. V. & Anashkina, E. A. Tunable Raman lasing in an As2S3 chalcogenide glass microsphere. *Opt. Express* **29**, 5580 (2021).
3. Shen, X., Choi, H., Chen, D., Zhao, W. & Armani, A. M. Raman laser from an optical resonator with a grafted single-molecule monolayer. *Nat. Photonics* **14**, 95–101 (2020).
4. Spillane, S. M., Kippenberg, T. J. & Vahala, K. J. Ultralow-threshold Raman laser using a spherical dielectric microcavity. *Nature* **415**, 621–623 (2002).
5. Rong, H. et al. An all-silicon Raman laser. *Nature* **433**, 292–294 (2005).
6. Zhang, Y., Zhong, K. & Tsang, H. K. Raman lasing in multimode silicon racetrack resonators. *Laser Photon. Rev.* **15**, 2000336 (2021).
7. Xia, D. et al. Engineered Raman lasing in photonic integrated chalcogenide microresonators. *Laser Photon. Rev.* **16**, 2100443 (2022).
8. Liu, X. et al. Integrated continuous-wave aluminum nitride Raman laser. *Optica* **4**, 893 (2017).
9. Latawiec, P., Venkataraman, V., Shams-Ansari, A., Markham, M. & Lončar, M. Integrated diamond Raman laser pumped in the near-visible. *Opt. Lett.* **43**, 318 (2018).
10. Latawiec, P. et al. On-chip diamond Raman laser. *Optica* **2**, 924 (2015).
11. Wang, C. et al. High-Q microresonators on 4H-silicon-carbide-on-insulator platform for nonlinear photonics. *Light Sci. Appl.* **10**, 139 (2021).
12. Gong, L., Lin, S. & Huang, Z. Stimulated Raman scattering tomography enables label-free volumetric deep tissue imaging. *Laser Photon. Rev.* **15**, 2100069 (2021).
13. Yan, M. et al. Surface-enhanced dual-comb coherent Raman spectroscopy with nanoporous gold films. *Laser Photon. Rev.* **12**, 1800096 (2018).
14. Passaro, V. & De Leonardis, F. Investigation of SOI Raman lasers for mid-Infrared gas sensing. *Sensors* **9**, 7814–7836 (2009).
15. Zhang, Y., Zhong, K., Zhou, X. & Tsang, H. K. Broadband high-Q multimode silicon concentric racetrack resonators for widely tunable Raman lasers. *Nat. Commun.* **13**, 3534 (2022).
16. Ahmadi, M., Shi, W. & LaRochelle, S. Widely tunable silicon Raman laser. *Optica* **8**, 804 (2021).
17. Rong, H. et al. A cascaded silicon Raman laser. *Nat. Photonics* **2**, 170–174 (2008).
18. Dimitrievska, M. et al. Multiwavelength excitation Raman scattering study of polycrystalline kesterite Cu2ZnSnS4 thin films. *Appl. Phys. Lett.* **104**, 021901 (2014).
19. Dimitrievska, M. et al. Multiwavelength excitation Raman scattering of Cu2ZnSn(SxSe1−x)4 (0 ≤ x ≤ 1) polycrystalline thin films: vibrational properties of sulfoselenide solid solutions. *Appl. Phys. Lett.* **105**, 031913 (2014).
20. Zhang, D. L., Hua, P. R., Yue-Bun Pun, E. & Siu, G. G. X-Ray, micro-Raman, optical absorption/emission studies of ErNbO4 grown by vapor transport equilibration. *J. Am. Ceram. Soc.* **90**, 2893–2899 (2007).
21. Rout, D., Subramanian, V., Hariharan, K. & Sivasubramanian, V. A comparative study of dielectric and Raman spectroscopy of Pb(Yb1/2Ta1/2)O3 and Pb(Yb1/2Nb1/2)O3. *Solid State Commun.* **141**, 192–197 (2007).
22. Shi, L. et al. The composition dependence and new assignment of the Raman spectrum in lithium tantalate. *Solid State Commun.* **135**, 251–256 (2005).
23. Schaufele, R. F. & Weber, M. J. Raman scattering by Lithium Niobate. *Phys. Rev.* **152**, 705 (1966).
24. Kaminow, I. P. & Johnston, W. D. Quantitative determination of sources of the electro-optic effect in LiNbO₃. *Phys. Rev.* **160**, 519 (1967).
25. Barker, A. S. & Loudon, R. Dielectric properties and optical phonons in LiNbO3. *Phys. Rev.* **158**, 433 (1967).
26. Repelin, Y., Husson, E., Bennani, F. & Proust, C. Raman spectroscopy of lithium niobate and lithium tantalate. Force field calculations. *J. Phys. Chem. Solids* **60**, 819–825 (1999).
27. Caciuc, V., Postnikov, A. & Borstel, G. Ab initio structure and zone-center phonons in LiNbO3. *Phys. Rev. B* **61**, 8806 (2000).
28. Yu, M. et al. Raman lasing and soliton mode-locking in lithium niobate microresonators. *Light Sci. Appl.* **9**, 9 (2020).
29. Fujii, S., Kato, T., Suzuki, R., Hori, A. & Tanabe, T. Transition between Kerr comb and stimulated Raman comb in a silica whispering gallery mode microcavity. *J. Opt. Soc. Am. B* **35**, 100 (2018).
30. Liu, Y. et al. Investigation of mode coupling in normal-dispersion silicon nitride microresonators for Kerr frequency comb generation. *Optica* **1**, 137 (2014).
31. Xue, X. et al. Mode-locked dark pulse Kerr combs in normal-dispersion microresonators. *Nat. Photonics* **9**, 594–600 (2015).
32. Xue, X. et al. Normal-dispersion microcombs enabled by controllable mode interactions. *Laser Photon. Rev.* **9**, L23–L28 (2015).
33. Jang, J. K. et al. Dynamics of mode-coupling-induced microresonator frequency combs in normal dispersion. *Opt. Express* **24**, 28794 (2016).
34. Fujii, S. et al. Analysis of mode coupling assisted Kerr comb generation in normal dispersion system. *IEEE Photonics J.* **10**, 1–11 (2018).

35. Zhang, Y. et al. Sub-milliwatt optical frequency combs in dual-pumped high-Q multimode silicon resonators. *Appl. Phys. Lett.* **117**, 221103 (2020).

36. Huang, S.-W. et al. Smooth and flat phase-locked Kerr frequency comb generation by higher order mode suppression. *Sci. Rep.* **6**, 26255 (2016).

37. Miller, S. A. et al. Tunable frequency combs based on dual microring resonators. *Opt. Express* **23**, 21527 (2015).

38. Boes, A. et al. Lithium niobate photonics: unlocking the electromagnetic spectrum. *Science* **379**, eabj4396 (2023).

39. Zhu, D. et al. Integrated photonics on thin-film lithium niobate. *Adv. Opt. Photonics* **13**, 242 (2021).

40. Chen, G. et al. Advances in lithium niobate photonics: development status and perspectives. *Adv. Photonics* **4**, 034003 (2022).

41. Beckmann, T. et al. Highly tunable low-threshold optical parametric oscillation in radially poled whispering gallery resonators. *Phys. Rev. Lett.* **106**, 143903 (2011).

42. Myers, L. E. et al. Quasi-phase-matched 1064-μm-pumped optical parametric oscillator in bulk periodically poled LiNbO_3. *Opt. Lett.* **20**, 52 (1995).

43. Wei, D. et al. Experimental demonstration of a three-dimensional lithium niobate nonlinear photonic crystal. *Nat. Photonics* **12**, 596–600 (2018).

44. Strößner, U. et al. Single-frequency continuous-wave optical parametric oscillator system with an ultrawide tuning range of 550 to 2830 nm. *J. Opt. Soc. Am. B* **19**, 1419 (2002).

45. Webjörn, J., Laurell, F. & Arvidsson, G. Fabrication of periodically domain-inverted channel waveguides in lithium niobate for second harmonic generation. *J. Light. Technol.* **7**, 1597–1600 (1989).

46. Wooten, E. L. et al. Review of lithium niobate modulators for fiber-optic communications systems. *IEEE J. Sel. Top. Quantum Electron.* **6**, 69–82 (2000).

47. Langrock, C. et al. Highly efficient single-photon detection at communication wavelengths by use of upconversion in reverse-proton-exchanged periodically poled LiNbO_3 waveguides. *Opt. Lett.* **30**, 1725 (2005).

48. Jin, H. et al. On-chip generation and manipulation of entangled photons based on reconfigurable lithium-niobate waveguide circuits. *Phys. Rev. Lett.* **113**, 103601 (2014).

49. Langrock, C., Kumar, S., McGeehan, J. E., Willner, A. E. & Fejer, M. M. All-optical signal processing using χ(2) nonlinearities in guided-wave devices. *J. Light. Technol.* **24**, 2579–2592 (2006).

50. Zhang, M., Wang, C., Cheng, R., Shams-Ansari, A. & Lončar, M. Monolithic ultra-high-Q lithium niobate microring resonator. *Optica* **4**, 1536 (2017).

51. Rabiei, P. & Gunter, P. Optical and electro-optical properties of submicrometer lithium niobate slab waveguides prepared by crystal ion slicing and wafer bonding. *Appl. Phys. Lett.* **85**, 4603 (2004).

52. Hu, H., Ricken, R. & Sohler, W. Lithium niobate photonic wires. *Opt. Express* **17**, 24261 (2009).

53. Chang, L. et al. Thin film wavelength converters for photonic integrated circuits. *Optica* **3**, 531 (2016).

54. Ling, J. et al. Athermal lithium niobate microresonator. *Opt. Express* **28**, 21682 (2020).

55. Luke, K. et al. Wafer-scale low-loss lithium niobate photonic integrated circuits. *Opt. Express* **28**, 24452 (2020).

56. Zhang, M. et al. Broadband electro-optic frequency comb generation in a lithium niobate microring resonator. *Nature* **568**, 373–377 (2019).

57. Wang, C. et al. Monolithic lithium niobate photonic circuits for Kerr frequency comb generation and modulation. *Nat. Commun.* **10**, 978 (2019).

58. He, Y. et al. Self-starting bi-chromatic LiNbO 3 soliton microcomb. *Optica* **6**, 1138 (2019).

59. Gong, Z., Liu, X., Xu, Y. & Tang, H. X. Near-octave lithium niobate soliton microcomb. *Optica* **7**, 1275 (2020).

60. Wang, C. et al. Integrated lithium niobate electro-optic modulators operating at CMOS-compatible voltages. *Nature* **562**, 101–104 (2018).

61. Aoki, K. et al. Single-drive X-cut thin-sheet LiNbO3 optical modulator with chirp adjusted using asymmetric CPW electrode. *J. Light. Technol.* **24**, 2233–2237 (2006).

62. He, M. et al. High-performance hybrid silicon and lithium niobate Mach–Zehnder modulators for 100 Gbit s−1 and beyond. *Nat. Photonics* **13**, 359–364 (2019).

63. Ledezma, L. et al. Intense optical parametric amplification in dispersion-engineered nanophotonic lithium niobate waveguides. *Optica* **9**, 303 (2022).

64. Jankowski, M. et al. Quasi-static optical parametric amplification. *Optica* **9**, 273 (2022).

65. Wolf, R. et al. Quasi-phase-matched nonlinear optical frequency conversion in on-chip whispering galleries. *Optica* **5**, 872 (2018).

66. Lu, J. et al. Periodically poled thin-film lithium niobate microring resonators with a second-harmonic generation efficiency of 250,000%/W. *Optica* **6**, 1455 (2019).

67. Chen, J. et al. Ultra-efficient frequency conversion in quasi-phase-matched lithium niobate microrings. *Optica* **6**, 1244 (2019).

68. McKenna, T. P. et al. Ultra-low-power second-order nonlinear optics on a chip. *Nat. Commun.* **13**, 4532 (2022).

69. Jankowski, M. et al. Ultrabroadband nonlinear optics in nanophotonic periodically poled lithium niobate waveguides. *Optica* **7**, 40 (2020).

70. Guo, Q. et al. Femtojoule femtosecond all-optical switching in lithium niobate nanophotonics. *Nat. Photonics* **16**, 625–631 (2022).

71. Liu, X. et al. Tunable single-mode laser on thin film lithium niobate. *Opt. Lett.* **46**, 5505 (2021).

72. Simons, M. T. & Novikova, I. Observation of second-order hyper-Raman generation in LiNbO_3 whispering-gallery mode disk resonators. *Opt. Lett.* **36**, 3027 (2011).

73. Leidinger, M., Sturman, B., Buse, K. & Breunig, I. Strong forward-backward asymmetry of stimulated Raman scattering in lithium-niobate-based whispering gallery resonators. *Opt. Lett.* **41**, 2823 (2016).

74. Moore, J., Tomes, M., Carmon, T. & Jarrahi, M. Continuous-wave cascaded-harmonic generation and multi-photon Raman lasing in lithium niobate whispering-gallery resonators. *Appl. Phys. Lett.* **99**, 221111 (2011).

75. Wu, R. et al. Lithium niobate micro-disk resonators of quality factors above 10 7. *Opt. Lett.* **43**, 4116 (2018).

76. Wolf, R., Breunig, I., Zappe, H. & Buse, K. Cascaded second-order optical nonlinearities in on-chip micro rings. *Opt. Express* **25**, 29927 (2017).

77. Jung, H. et al. Stokes and anti-Stokes Raman scatterings from frequency comb lines in poly-crystalline aluminum nitride microring resonators. *Opt. Express* **27**, 22246 (2019).

78. Gong, Z. et al. Photonic dissipation control for Kerr soliton generation in strongly Raman-active media. *Phys. Rev. Lett.* **125**, 183901 (2020).

79. Kippenberg, T. J., Spillane, S. M., Min, B. & Vahala, K. J. Theoretical and experimental study of stimulated and cascaded Raman scattering in ultrahigh-Q optical microcavities. *IEEE J. Sel. Top. Quantum Electron.* **10**, 1219–1228 (2004).

80. Liang, W. et al. Generation of a coherent near-infrared Kerr frequency comb in a monolithic microresonator with normal GVD. *Opt. Lett.* **39**, 2920 (2014).

81. Nazemosadat, E. et al. Switching dynamics of dark-pulse Kerr frequency comb states in optical microresonators. *Phys. Rev. A* **103**, 013513 (2021).

82. Ji, X. et al. Compact, spatial-mode-interaction-free, ultralow-loss, nonlinear photonic integrated circuits. *Commun. Phys.* **5**, 84 (2022).

83. Haus, H. A. & Huang, W. Coupled-mode theory. *Proc. IEEE* **79**, 1505–1518 (1991).

84. Ye, C. et al. Robust multimode waveguide design for avoided mode crossing-suppressed microresonators. *J. Light. Technol.* **41**, 1–6 (2023).

85. Kim, C. et al. Design and fabrication of AlGaAs-on-insulator microring resonators for nonlinear photonics. *IEEE J. Sel. Top. Quantum Electron.* **29**, 1–13 (2023).

86. Chen, G., Lin, H. L., Da Ng, J. & Danner, A. J. Integrated thermally tuned Mach-Zehnder interferometer in z-Cut lithium niobate thin film. *IEEE Photonics Technol. Lett.* **33**, 664–667 (2021).

87. Jin, W., Chiang, K. S. & Liu, Q. Thermally tunable lithium-niobate long-period waveguide grating filter fabricated by reactive ion etching. *Opt. Lett.* **35**, 484 (2010).

88. Soltanian, E. et al. Micro-transfer-printed narrow-linewidth III-V-on-Si double laser structure with a combined 110 nm tuning range. *Opt. Express* **30**, 39329 (2022).

89. Kobayashi, N. et al. Silicon photonic hybrid ring-filter external cavity wavelength tunable lasers. *J. Light. Technol.* **33**, 1241–1246 (2015).

90. Xiang, C. et al. High-performance silicon photonics using heterogeneous integration. *IEEE J. Sel. Top. Quantum Electron.* **28**, 1–15 (2022).

91. Yang, C. et al. Advances in silicon-based, integrated tunable semiconductor lasers. *Nanophotonics* **12**, 197–217 (2023).

Author contributions

Y.Z. and M.P. conceived the idea. Y.Z. conducted the simulations and experiments. X.L. fabricated the samples. Y.Z. and M.P. analyzed the data and discussed the results with K.Y., X.C.Y.Z., and M.P. prepared the paper with input from all the co-authors. K.Y., X.C., and M.P. supervised the project.

Competing interests

Additional information

Supplementary information The online version contains supplementary material available at https://doi.org/10.1038/s42005-023-01477-6.

Correspondence and requests for materials should be addressed to Xinlun Cai or Minhao Pu.

Peer review information *Communications Physics* thanks the anonymous reviewers for their contribution to the peer review of this work. A peer review file is available.

Reprints and permission information is available at http://www.nature.com/reprints

Publisher's note Springer Nature remains neutral with regard to jurisdictional claims in published maps and institutional affiliations.